Inorganic Chemistry

Article

pubs.acs.org/IC

Effect of Axial Ligand on the Electronic Configuration, Spin States, and Reactivity of Iron Oxophlorin

Mahin Gheidi, Nasser Safari,* and Mansour Zahedi

Department of Chemistry, Faculty of Sciences, Shahid Beheshti University, G.C., Evin, 19839-63113, Tehran, Iran

Supporting Information

ABSTRACT: Iron-oxophlorin is an intermediate in heme degradation, and the nature of the axial ligand can alter the spin, electron distribution, and reactivity of the metal and the oxophlorin ring. The structure and reactivity of iron-oxophlorin in the presence of imidazole, pyridine, and *t*-butyl isocyanide as axial ligands was investigated using the B3LYP and OPBE methods with the 6-31+G* and 6-311+G** basis sets. OPBE/6-311+G** has shown that the doublet state of $[(Py)_2Fe^{III}(PO)]$ (where pyridines are in perpendicular planes and PO is the oxophlorin trianion) is 3.45 and 5.27 kcal/mol more stable than the quartet and sextet states, respectively. The ground-state electronic configuration of the aforementioned complex is $\pi_{xz}^2\ \pi_{yz}^2\ a_{2u}^2\ d_{xy}^1$ at low temperatures and changes to $\pi_{xz}^2\ \pi_{yz}^2\ d_{xy}^2\ a_{2u}^1$ at high temperatures. This latter electronic configuration is consistently seen for the $[(t\text{-BuNC})_2Fe^{II}(PO^{\bullet})]$ complex (where $PO^{\bullet}$ is the oxophlorin dianion radical). The complex $[(Im)_2Fe^{III}(PO)]$ adopted the $d_{xy}^2\ (\pi_{xz}\ \pi_{yz})^3$ ground state and has low-lying quartet excited state which is readily populated when the temperature is increased.

INTRODUCTION

Heme oxygenase converts unwanted heme to biliverdin in animals and birds.[1−3] Two major intermediates isolated and characterized in this heme oxygenase process or in coupled oxidation model system are oxophlorin and verdoheme[4−9] (see Scheme 1).

Conversion of heme to biliverdin has especially been studied in biological systems[10−15] and in models called coupled oxidation during the last two decades.[9,16−18] These experimental and theoretical works have shed light on the details of the conversion of heme to oxophlorin and the conversion of verdoheme to biliverdin.[19−23]

However, there is a lack of information on the transformation of oxophlorin to verdoheme. It is known that oxophlorin is air-sensitive and in the presence of O_2 transforms to the biliverdin by releasing carbon monoxide (CO). Balch and co-workers have indeed characterized complexes of oxophlorin macrocycles in model systems called coupled oxidation.[24−29] They have shown that, in iron complexes of oxophlorin macrocycles, this is a vexing problem in view of the apportionment of electrons between iron and macrocycles. Scheme 2 shows three major resonances proposed for iron oxophlorins.

Different experimental evidence has been presented which favors Fe(I), while, elsewhere, formulations of Fe(II) and Fe(III) have been reported. Recently, it has been documented that the axial ligands have profound effects on the nature of the iron oxidation states and oxophlorin macrocycles.[28,29] There is spectroscopic and crystallographic evidence which shows in the presence of an isocyanide ligand, the complex exists in the form of $(RNC)_2Fe^{II}(OEPO^{\bullet})$ (where $OEPO^{\bullet}$ is the octaethyloxophlorin dianion radical). In the aforementioned complex the iron is diamagnetic low spin and unpaired electrons are centered on the macrocycle.[27,28] The complexes of $(Im)_2Fe^{III}(OEPO)$ (where OEPO is the octaethyloxophlorin trianion) indicate an Fe(III) low-spin state both in the solid state and in the solution in variable temperatures. The solid structures of the $(Im)_2Fe^{III}(OEPO)$ show that the imidazoles are almost perpendicular to each other. Otherwise, $(Py)_2Fe^{III}(OEPO)$ has been confirmed to have an Fe(III) oxidation state, which is high spin from 4 k to 300 k in the solid state. Furthermore, the pyridines lie in a common plane.[29] Surprisingly, in solution, this complex has shown different behavior and is proposed to be low-spin Fe(III).

Therefore, the spin states of iron represent another parameter besides the electronic states that must be determined. In addition, experimental evidence has shown that complexes of L_2Fe (OEPO) are air-sensitive, but its products with O_2 would change based on the chemistry imposed by L ligands. With isocyanide ligands, the reaction stops at the verdoheme stage; however, with pyridine ligands, iron biliverdin is formed.

Despite excellent experimental work on iron oxophlorins and other metallo-oxophlorins, the details of electronic and spin distribution between iron and the macrocycles still must be determined and analyzed to shed light on the reactive form of the oxophlorins. We believe theoretical methods can add valuable information to the experimental works to clarify the exact nature of oxophlorin in biology. The exact determination of the reactive macrocycle in oxophlorin states is essential to understanding the mechanism of conversion of oxophlorin macrocycle to verdoheme.

METHODS

Density functional theory (DFT) methods were employed using the B3LYP and OPBE hybrid density functional methods,[30] as implemented in the Gaussian 2003(A.B.3)[31] program series. We have used B3LYP and OPBE methods[32,33] and 6-31+G*, 6-311+G**[34,35] basis functions in this investigation; the B3LYP/6-31+G* method is used

Received: November 23, 2011
Published: June 11, 2012

Scheme 1

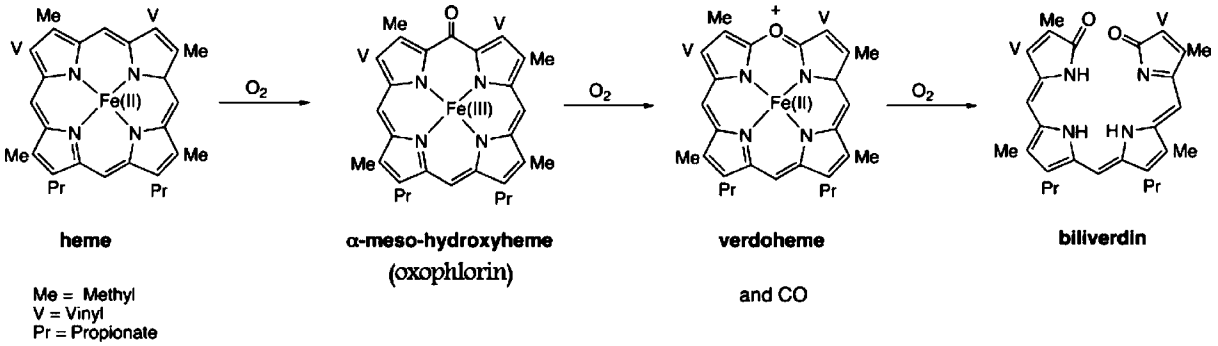

Scheme 2

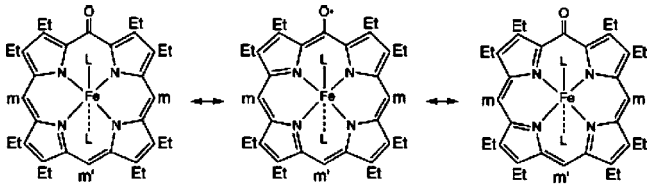

for the optimization of all structures. Single point energies for DFT functional (B3LYP, OPBE) were obtained at OPBE optimized geometries using the 6-311+G** basis set. It is well-known that the 6-31+G* basis set tends to predict high-spin states at energies that are too low. Therefore, we included energies with a reliable basis set, 6-311+G**. The spin-unrestricted version of the B3LYP (UB3LYP) method was even applied to singlet states when the reaction species are considered to have an open-shell-singlet electronic configuration.[36−40]

A subsequent analytical frequency calculation characterized the structures as local minima with real frequencies only or a transition state that had just one imaginary frequency. All energies reported in this work used the latter basis set and were corrected for zero-point energies as taken from the frequency calculations. Atomic charge and spin density studies were based on the Mulliken calculation. The natural bond orbital (NBO) analysis is used to explain electron distribution in the d orbitals of iron and the macrocycle ring, as well as to assign the atomic charges. The molecular orbital analyses were performed by the Gauss View that was applied to the respective Gaussian output file.

The model of the oxophlorin site used in all DFT calculations is an iron oxophlorin complex taken from the crystal structure of the iron complexes of octaethyloxophlorin,[25,27,29] after substituting the ethyl group with hydrogen (abbreviated as PO).

RESULTS AND DISCUSSION

In contrast to the large body of experimental work in recent years on the heme cleavage system, little attention has been paid to the theoretical investigation of this important biological process. In this study, an ab initio density functional theory (DFT) method was employed to investigate the effect of axial ligands on the reactivity of oxophlorin in the heme degradation process with pyridine (Py), imidazole (Im), and *t*-butyl isocyanide (*t*-BuNC) as axial ligands: $[L_2Fe(PO)]^0$ (L = Im, Py, *t*-BuNC).

Before discussing the reactivity patterns as a function of the axial ligands, we first considered the optimized geometries of the reactant complexes where we optimized ($\mathbf{R}_L$) in the doublet, quartet, and sextet spin states (Figures 1 and 5). In this nomenclature, the axial ligand (L) is given in subscript after the label and the spin multiplicity as a superscript before the label.

It is found that both DFT/B3LYP and OPBE methods predict the structural and electronic properties of iron oxophlorin complexes in preselected spin-electronic states and are in very good agreement with X-ray and magnetic experimental data, even when applied in conjunction with a rather modest basis sets. 6-31+G* and 6-311+G** were utilized as basis sets, since calculations at these levels of theory have been shown to give accurate results, from the geometry and spin evaluation points of view.[35] However, the B3LYP method was not adequate to predict the spin ground-state energies in accord with the experiment. For all complexes, OPBE predicts the correct spin ground state. Furthermore, in a series of papers, Ghosh and co-workers[41−43] have clearly demonstrated that OPBE seems to give good results, not only for iron complexes but also for other transition metals.

Geometries and energies of $\mathbf{R}_L$ with L = Py, Im, and *t*-BuNC were fully optimized and computed in all the spin states. Table 1 shows the computed relative energy stabilization for these compounds.

The details of the bond distances for all compounds by OPBE method are given in Table 2, and the optimized

Table 1. Calculated Relative Energies for All of Compounds Using B3LYP and OPBE/6-311+G** Methods[a]

		Energy Stabilization (kcal/mol)					
		B3LYP			OPBE		
compound	orientation	doublet	quartet	sextet	doublet	quartet	sextet
$(Im)_2Fe^{III}(PO)$	⊥	0.00	4.16	5.68	0.00	2.32	5.33
$(Im)_2Fe^{III}(PO)$	//			6.02		3.02	5.60
$(Py)_2Fe^{III}(PO)$	⊥	3.70	0.00	3.72	0.00	3.45	5.27
$(Py)_2Fe^{III}(PO)$	//	7.44	3.51	4.06	6.27	4.89	6.08
$(t\text{-BuNC})_2Fe^{II}(PO^{\bullet})$		0.00	20.20	15.41	0.00	18.40	15.07

[a]The symbol "⊥" denotes when pyridines and imidazoles are in the perpendicular plane. The symbol "//" denotes for when pyridines and imidazoles are in the common plane.

dx.doi.org/10.1021/ic202527u | Inorg. Chem. 2012, 51, 7094−7102

Table 2. Calculated Selected Bond Distances for Iron Oxophlorin Complexes Using the OPBE/6-31+G* Method

	Bond Distance (Å)					
	Fe-L		Fe−$N_{ave.ring}$		C−O	
[L_2Fe(PO)]	⊥	X-ray		X-ray		X-ray
L = Im						
doublet	1.99	1.97	2.01	2.00	1.27	1.28
quartet	2.25		2.01		1.27	
sextet	2.21		2.09		1.27	
L = Py						
doublet	2.03		2.02		1.27	
quartet	2.31		2.01		1.27	
sextet	2.28	2.26	2.08	2.05	1.27	1.28
L = *t*-BuNC						
doublet	1.89	1.89	2.03	2.01	1.28	1.35
quartet	1.89		2.10		1.27	
sextet	2.26		2.10		1.27	

structures by B3LYP method are presented in the Supporting Information.

Charge densities and spin distributions for all compounds are presented in Table 3.

[$(Py)_2$ Fe^{III}(PO)]. The structure of R_{Py} was fully optimized and computed correctly with the pyridine groups in parallel and perpendicular planes in all spin states. In some cases, B3LYP is unable to predict the ground-spin state of the complexes. Namely, B3LYP has shown that the ground state of R_{Py} (with perpendicular pyridines) is the quartet state; OPBE/6-311+G**, however, shows that the doublet state is 3.45 and 5.27 kcal/mol more stable than the quartet and sextet states, respectively (see Table 1). The key geometric parameters of the optimized structure for R_{Py} are collected in Table 2. Figure 1 shows an image of the structure from the data obtained by the OPBE method at doublet, quartet and sextet spin states. (The data obtained by B3LYP are presented in the Supporting Information.) Balch and co-workers have shown that [$(Py)_2Fe^{III}$(OEPO)] exists in the high spin state in the solid state and in a low-spin form in solution. They also found that, in the solid state, the pyridines are on parallel planes.[29]

In the $^6R_{Py}$ with parallel pyridines the Fe−N_{ax} distance is 2.28 Å and the average Fe−N_{eq} distance is 2.08 Å. In the crystal structure, the Fe−N_{ax} distance is 2.26 Å, and the average Fe−N_{eq} distance is 2.05 Å, and the axial pyridines are parallel. In the $^2R_{Py}$ with perpendicular pyridines, one of the pyridines rotates around the *z*-axis to produce two parallel pyridines in $^2R_{Py}$ complex that has been destabilized by ∼6.27 kcal/mol. The barrier of rotation calculated with the OPBE method is 6.95 kcal/mol on the doublet surface (see Figure 1). In the quartet and sextet states, pyridine groups in parallel and perpendicular are almost degenerate. There is no difference in the preference for parallel or perpendicular orientations of pyridines for both quartet and sextet states, because they have the similar energies.

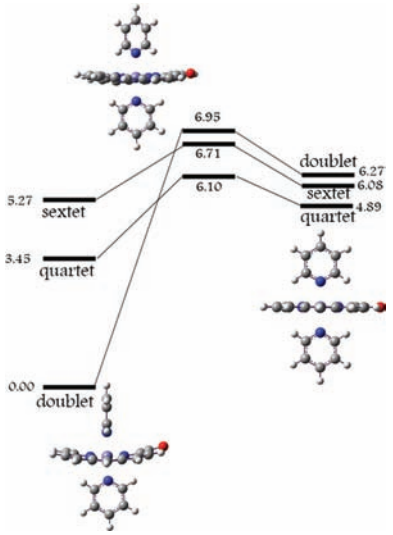

Figure 1. Energy diagram for conversion of R_{Py} with perpendicular pyridine to R_{Py} with parallel pyridine.

No practical barrier of rotation was found for axial pyridine ligands in the gas phase. In the crystal structure, however, crystal forces cause preference for parallel orientation and restrict the rotation of the pyridines toward perpendicular orientation. Since the beta-ethyl groups of OEPO were removed for the simplicity of calculation, we obtained rotation barrier of complex of [$(Py)_2Fe^{III}$ (OEPO)] in the doublet state as well. The barrier of rotation was calculated to be 6.95 kcal/mol for ^{2}[$(Py)_2Fe^{III}$ (PO)] and 7.80 kcal/mol for ^{2}[$(Py)_2Fe^{III}$ (OEPO)]. Thus, substituted ethyls have no significant effect on the rotation barrier of axial ligands (see Figure S1 in the Supporting Information).

In gas and solution phases, perpendicular orientation is preferred[29] in the ground state; complex R_{Py} has a low-spin doublet state $^2R_{Py}$, in which pyridines are perpendicular. Calculations show that two alternative electronic configurations are possible: $\pi_{xz}^2\,\pi_{yz}^2\,a_{2u}^2\,d_{xy}^1$ and $\pi_{xz}^2\,\pi_{yz}^2\,d_{xy}^2\,a_{2u}^1$ (see Figure 2a); these may be labeled as $^2[R_{Py}]_{xy}$ and $^2[R_{Py}]_{a2u}$, respectively. Closely lying states are the quartet state, $^4R_{Py}$ with the $d_{xy}^2\,d_{xz}^1\,d_{yz}^1\,\sigma^*_{z2}{}^1$ configuration, and a sextet state, $^6R_{Py}$ with $d_{xy}^1\,d_{xz}^1\,d_{yz}^1\,\sigma^*_{z2}{}^1\,\sigma^*_{x2-y2}{}^1$ orbital occupation. Low-spin ground states are found in all of these gas-phase model calculations to be $^2[R_{Py}]_{xy}$. The $^2[R_{Py}]_{a2u}$ state lies at only 3.9 kcal/mol higher than $^2[R_{Py}]_{xy}$ at a temperature of 273 K. As the temperature is increased, the $^2[R_{Py}]_{a2u}$ state becomes stabilized and populated. In $^{4,6}R_{Py}$, the oxophlorin group is close to planarity and two alternative pyridines orientations are possible: parallel and perpendicular (see Figure 1). In contrast, the structure of $^2[R_{Py}]_{xy}$ and $^2[R_{Py}]_{a2u}$ show a ruffled distortion of the oxophlorin and both have axial pyridines in perpendicular planes. Ruffled structures have been seen experimentally in the crystal structures of low-spin complexes [$(Im)_2Fe^{III}$(OEPO)].[29]

Table 3. Calculated Mulliken Spin and Charges Densities for the Fe, O, C_{oxo}, and C_{meso} Atoms and the Ring Macrocycle[a]

compound	Fe	ring	O	C_{oxo}	*meso* carbons	*meso* carbons trans
$^2[R_{Py}]_{xy}$	1.05 (1.57)	−0.03 (−1.56)	0.29 (−0.41)	0.15 (0.23)	0.13 (0.04)	0.27 (0.04)
$^2[R_{Py}]_{a2u}$	0.06 (1.21)	0.93 (−1.18)	0.03 (−0.50)	0.03 (−0.21)	0.01 (−0.02)	0.01 (−0.05)
$^2R_{Im}$	1.00 (1.55)	0.00 (−1.55)	0.04 (−0.50)	0.01 (0.22)	0.02 (0.04)	0.00 (0.06)
$^2[R_{t\text{-}BuCN}]_{a2u}$	0.00 (1.07)	1.00 (−1.03)	0.25 (−0.47)	0.10 (−0.23)	0.16 (0.00)	0.29 (0.00)

[a]Values shown in parentheses are charges densities.

dx.doi.org/10.1021/ic202527u | *Inorg. Chem.* 2012, 51, 7094−7102

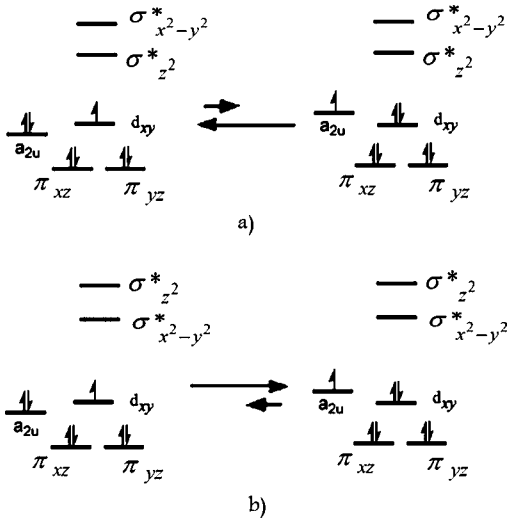

Figure 2. Orbital occupations for (a) $^2R_{Py}$ and (b) $^2R_{t\text{-BuNC}}$.

Charge densities and spin distributions for $^2R_{Py}$ are presented in Table 3. Therefore, the ring in $^2[R_{Py}]_{a2u}$ has a radical nature, since the charge density on the oxophlorin is −1.18 and the spin distribution is 0.93 while, in $^2[R_{Py}]_{xy}$, the charge on the oxophlorin is −1.56 and the spin density is −0.03. At higher temperatures, therefore, one electron is shifted from the macrocycle ring to iron, which results in the Fe(II) π dianion radical species $^2[R_{Py}]_{a2u}$. The radical nature of macrocycles in $^2[R_{Py}]_{a2u}$, which is populated in temperatures above 273 K, possibly makes the complex R_{Py} a highly reactive species in the heme degradation process.

To further confirm the electronic structures, we performed NBO analysis for $^2R_{Py}$. Table 4 shows the result of NBO analysis. NBO analysis for $^2[R_{Py}]_{a2u}$ is presented in Table 4a. These data reveal that the occupancy numbers of the alpha and beta spin orbitals for iron are, respectively, 2.83 and 2.71, resulting in a net alpha spin of 0.12 on the iron. In addition, one unpaired electron with alpha orientation is present on the macrocycle to make the entire system an Fe(II) d^6 with a dianionic macrocycle radical. Table 4b for $^2[R_{Py}]_{xy}$ also shows that the occupancy number of the alpha spin orbital for iron is 2.88 and that of the beta spin orbital of iron is 1.87 with a net alpha spin of 1.01 on the iron. Therefore, $^2[R_{Py}]_{xy}$ can be viewed as a low-spin Fe(III) with $S = {}^1/_2$ sitting in the ring of trianionic macrocycle (PO).

Table 4. NBO Analysis of Electron Distribution in Iron Atom (a) $^2[R_{Py}]_{a2u}$, (b) $^2[R_{Py}]_{xy}$, and (c) $^2[R_{t\text{-BuNC}}]_{a2u}$

Alpha Spin Orbital		Beta Spin Orbital	
occupancy	orbital	occupancy	orbital
(a) $^2[R_{Py}]_{a2u}$			
0.97012	LP (1)Fe	−0.91950	LP (1)Fe
0.95740	LP (2)Fe	−0.90459	LP (2)Fe
0.90500	LP (3)Fe	−0.88653	LP (3)Fe
sum of alpha spin electron		sum of beta spin electron	
2.83252		−2.71062	
(b) $^2[R_{Py}]_{xy}$			
0.98726	LP (1)Fe	−0.93470	LP (1)Fe
0.98164	LP (2)Fe	−0.93922	LP (2)Fe
0.91010	LP (3)Fe	−0.00000	LP (3)Fe
sum of alpha spin electron		sum of beta spin electron	
2.87900		−1.87392	
(c) $^2[R_{t\text{-BuNC}}]_{a2u}$			
0.97423	LP (1)Fe	−0.92304	LP (1)Fe
0.97117	LP (2)Fe	−0.91250	LP (2)Fe
0.95360	LP (3)Fe	−0.84402	LP (3)Fe
sum of alpha spin electron		sum of beta spin electron	
2.89900		−2.67956	

Our calculations in the gas phase also show that a significant change has occurred for axial pyridines, which are perpendicular in the doublet spin state and gradually turn to parallel orientation in the quartet and sextet states. Clearly, a spin state crossing from the doublet to the quartet and sextet spin states surface is required for the conversion of perpendicular to parallel pyridines in the R_{Py} (see Figure 1).

In addition, the orientation of the pyridine axial ligand causes major differences in the relative energies and will influence their electronic distribution. In Figure 3a, molecular orbital calculations show that, in $^{4,6}R_{Py}$ with parallel pyridines, Fe orbitals do not effectively overlap with π^*_x orbitals of pyridines and only axial pyridines effectively overlap with the oxophlorin ring. This can be the reason why, in the solid states, the pyridines are arranged in a parallel arrangement that eclipses a trans set of Fe−N (porphyrin) bonds and the oxophlorin is planar.[29] Any twisting of the ligands about the Fe−N bonds and the change in spin state are clearly inhibited in the solid state. Figure 3b demonstrates that, in $^2R_{Py}$ with perpendicular pyridines, both degenerate orbitals d_{xz} and d_{yz} of Fe overlap with π^*_x and π^*_y orbital of axial ligands, respectively. Because of this strong orbital overlap, pyridines cannot readily rotate around the Z-axis and have 6.95 kcal/mol rotation barriers. However, what causes the reorientation of the pyridines from perpendicular to the parallel one is unclear to us.

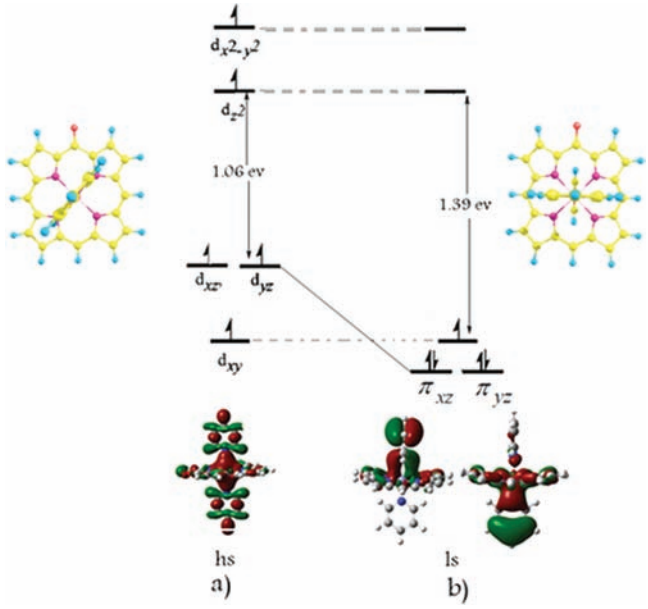

Figure 3. MO, KS, and MO diagram, relevant to (a) parallel pyridines in $^6R_{Py}$ and (b) perpendicular pyridines in $^2R_{Py}$.

In $^2[R_{Py}]_{xy}$, temperature causes one of the electrons to be promoted to a singly occupied d_{xy} orbital ($a_{2u}\rightarrow d_{xy}$), which results in the free radical species of $^2[R_{Py}]_{a2u}$. This unpaired

dx.doi.org/10.1021/ic202527u | Inorg. Chem. 2012, 51, 7094−7102

electron is localized on oxophlorin (see Figure 2). Figure 4 shows the electron distribution in the HOMO of the ring,

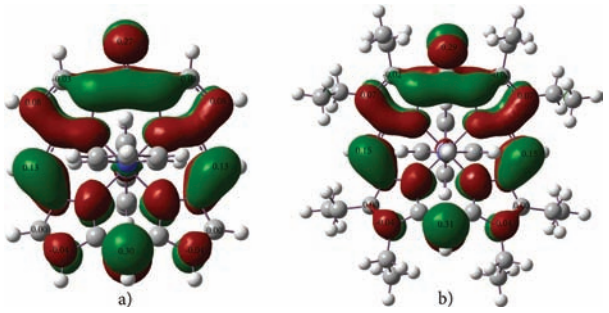

Figure 4. HOMO, KS, for the iron oxophlorin dianion radical with a_{2u} symmetry for (a) $^2[R_{Py}]_{a2u}$ and (b) $^2[(Py)_2Fe^{III}(OEPO)]_{a2u}$.

which has π^* character located on the C−O bond. This orbital, which is described in Figure 4a, will be singly occupied and corresponds to the well-known porphyrin a_{2u} orbital. By removing the electron from C−O π^*, this bond in $^2[R_{Py}]_{a2u}$ is shortened around 0.03 Å. Balch and co-workers showed and discussed that $^2[R_{Py}]_{a2u}$ has a larger C−O bond than $^2[R_{Py}]_{xy}$, which is in contrast with the result obtained in this work. However, the experimental results suffer from disorder in the C−O position.

[(Im)$_2$Fe^{III}(PO)]. The structure of R_{Im} was fully optimized and computed with the imidazole groups in parallel and perpendicular planes in all possible spin states, using B3LYP and OPBE/6-31+G* methods. Figure 5 shows a drawing of the

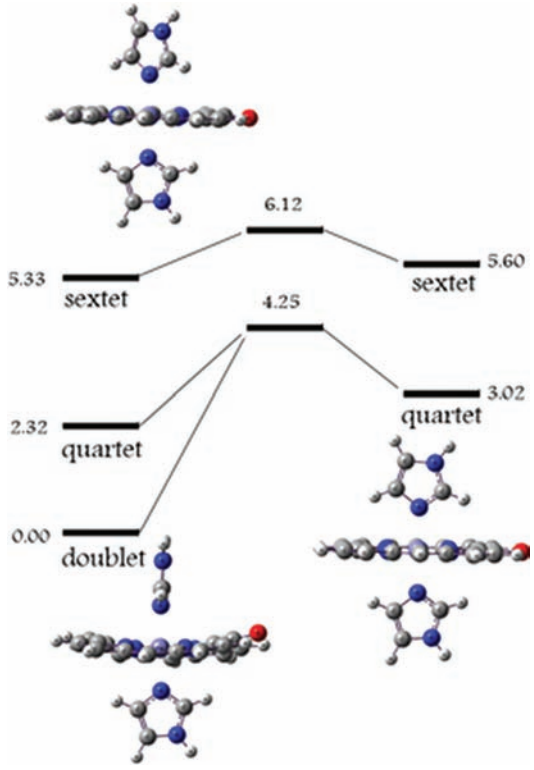

Figure 5. Energy diagram for conversion of R_{Im} with perpendicular imidazole to R_{Im} with parallel imidazole.

structure from the data obtained by the OPBE method at doublet, quartet, and sextet spin states. (The data obtained by B3LYP are presented in the Supporting Information). The ground state of R_{Im} is a doublet state with a singly occupied π_{xz} orbital. The quartet and sextet states are 2.32 and 5.33 kcal/mol higher than the doublet state at the OPBE/6-311+G** level. The configuration of the quartet and sextet state are, respectively, $d_{xy}^2\ \pi_{xz}^1\ \pi_{yz}^1\ \sigma^*_{z2}{}^1$ and $d_{xy}^1\ \pi_{xz}^1\ \pi_{yz}^1\ \sigma^*_{z2}{}^1\ \sigma^*_{x2-y2}{}^1$. The combined experimental−theoretical study of R_{Im} also shows that the observed structural parameters fit only those of the doublet spin state.

The key geometric parameters of the optimized structures for R_{Im} are collected in Table 2. In the ground state of $^2R_{Im}$, the axial Fe−N bond distance is 2.00 C and the average Fe−N_{eq} distance is 2.01 Å. (In the crystal structure, the Fe−N_{ax} distance is 1.97 Å and the average Fe−N_{eq} distance is 2.00 Å).

On the basis of geometry optimization in the doublet ground state, the energy minimum occurs at the geometry where the two Im are oriented nearly perpendicular with a 86.53° dihedral angle, which is also in close agreement with the 74.06° angle observed in the X-ray structure of R_{Im}.[29] Even starting from the parallel axial orientations of Im, the geometry optimization using DFT converged to the perpendicular axial. However in the quartet and sextet states, the two additional local minima with the imidazole groups in parallel and perpendicular planes exist in which the perpendicular orientation is more stable than the parallel orientation.

Experimental results show that [(Im)$_2$Fe^{III}(OEPO)] has doublet spin states in solid state and in solution. However, the magnetic moment of the sample gradually increased from 4 K to 300 K. In addition, [(Im)$_2$Fe^{III}(OEPO)], such as [(Py)$_2$Fe^{III}(OEPO)], has high spin state in crystalline form at room temperature, which undergoes spin exchange to low spin at low temperature. What is the basis of this spin exchange in the solid state and in solution and what is the role of temperature in this regard?

This theoretical study can shed light on this odd behavior in iron oxophlorin systems. Figure 5 demonstrates that, in $^{6,4}R_{Im}$ with perpendicular imidazoles, one of the imidazoles rotates around the z-axis to produce two parallel imidazoles in complex $^{6,4}R_{Im}$ that has been destabilized by ∼0.7 kcal/mol (in quartet) and 0.3 kcal/mol (in sextet) and the barrier of rotation, calculated with B3LYP, is ∼1.93 kcal/mol (in quartet) and 0.8 kcal/mol (in sextet). Thus, the parallel and perpendicular orientations for $^{6,4}R_{Im}$ are almost degenerate.

A somewhat subtle point concerns the electronic configuration of the lowest-energy $s = {}^3/_2$ state of R_{Im}. Careful examination of the MO occupancies reveals that the lowest-energy quartet derives from a $d\pi \rightarrow \sigma^*_{z2}$ excitation, rather than from a $d_{xy} \rightarrow \sigma^*_{z2}$ excitation. Approximately, the electronic configuration of the lowest-energy $s = {}^3/_2$ state (quartet spin state) of R_{Im} may be described as follows: $d_{xy}^2\ \pi_{xz}^1\ \pi_{yz}^1\ \sigma^*_{z2}{}^1$ (see Figure 8a).

[(t-BuNC)$_2$Fe^{II}(PO$^•$)]. For *t*-BuNC ligated to iron oxophlorin, the doublet spin state (ground state) is 20.20 kcal/mol more stable than the quartet spin state and 15.40 kcal/mol more stable than the sextet spin state. In the doublet state, two alternative electronic configurations are possible: $(\pi_{xz}, \pi_{yz})^4\ a_{2u}^2\ d_{xy}^1$ and $(\pi_{xz}, \pi_{yz})^4\ d_{xy}^2\ a_{2u}^1$. These may be labeled as $^2[R_{t\text{-BuNC}}]_{xy}$ and $^2[R_{t\text{-BuNC}}]_{a2u}$, respectively. This complex has a $^2[R_{t\text{-BuNC}}]_{a2u}$ ground state, with the $^2[R_{t\text{-BuNC}}]_{xy}$ state being 6.5 kcal/mol higher than the $^2[R_{t\text{-BuNC}}]_{a2u}$ ground state. One of the electrons may shift from doubly occupied d_{xy} orbital to a singly occupied a_{2u} orbital ($d_{xy} \rightarrow a_{2u}$), resulting in the formation

dx.doi.org/10.1021/ic202527u | Inorg. Chem. 2012, 51, 7094−7102

of $^2[R_{t\text{-BuNC}}]_{xy}$. Full optimization of this electronic structure was performed and the parameters are collected in Table 2. In the doublet spin state (ground state), the Fe−C distance of axial is 1.89 Å and the average Fe−N_{eq} distance is 2.03 Å (in the crystal structure, the Fe−C axial distance is 1.89 Å and the average Fe−N_{eq} distance is 2.01 Å). Furthermore, *t*-BuNC has the shortest ligand-to-metal bond. Because in this case, π-back bonding to the acceptor isocyanide ligands contributes to the stabilization of the low-spin Fe(II) state.

Figure 6 shows Kohn−Sham orbitals for the last 6 HOMOS of $R_{t\text{-BuNC}}$. Based on this figure, an unpaired electron is placed

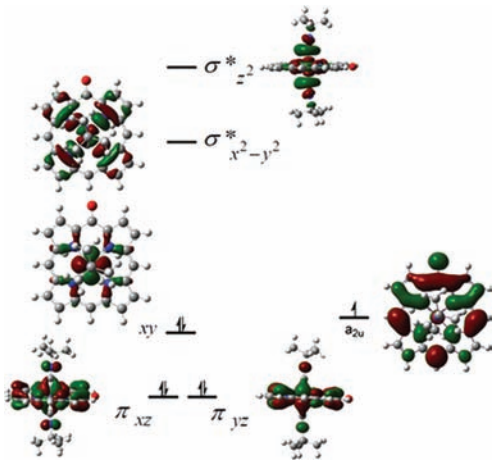

Figure 6. Kohn−Sham orbitals for the last 6 HOMOS of (*t*-BuNC)$_2$Fe^{II}(PO$^{\bullet}$) in the ground state.

on the a_{2u}-like orbital of the macrocycle and the electronic configuration of Fe is $(d_{xz}, d_{yz})^4 d_{xy}^2$. Therefore, the ring in $R_{t\text{-BuNC}}$ has a radical nature, since the charge density on the oxophlorin is −0.95 and spin distribution is 1.05. However, as shown in Figure 6, one of the electrons is shifted from the macrocycle ring to iron in $R_{t\text{-BuNC}}$, which results in the Fe(II) π dianion radical species. The radical nature of the macrocycle in $R_{t\text{-BuNC}}$ makes it air-sensitive, and it readily undergoes opening of the oxophlorin ligand to produce verdoheme, as is documented by experimental reports.[28]

In $R_{t\text{-BuNC}}$, two orbitals exhibit π-bonding interactions; these are π_{xz} and one of the π_{yz}, which get stabilized and descend below d_{xy}. The two high-lying virtual orbitals are σ^* orbitals; one (σ^*_{x2-y2}) describes the Fe−N antibonding interaction and the other (σ^*_{z2}), those along the N−C−Fe−C−N axis and when the Fe−C is short as in $R_{t\text{-BuNC}}$, σ^*_{z2} rise above σ^*_{x2-y2}.

Calculated spins show that the spin density on the iron is 0.1 and on the tetrapyrole ligand is 0.9. This electronic distribution is in accordance with the metal orbital splitting shown in Figure 6.

Data from the analysis of NBO in Table 4c show that the occupancy number of the α spin orbital for iron is 2.91 and that of the β spin orbital of iron is 2.68, which result in a net α spin of 0.23 on iron. Almost one unpaired electron with α is present on the macrocycle to make the entire system an Fe(II) d^6 with the macrocycle as a dianionic radical.

This is possibly due to π-back bonding to the acceptor isocyanide ligands, which contributes to the stabilization of the low-spin Fe(II) state. Therefore, because of the electronegativity of the iron in $R_{t\text{-BuNC}}$ relative to the iron in R_{Py} and R_{Im} one electron transfers mainly on the iron of $R_{t\text{-BuNC}}$ and the charge on the iron decreases from 1.56 in $(Py)_2Fe^{II}(PO^{\bullet})$ to 1 in $(t\text{-BuNC})_2Fe^{II}(PO^{\bullet})$.

Effect of Axial π-Bonding on the Character of the Electronic Ground State. The key role of π-bonding interactions of nitrogenous axial ligands on electron distribution and spin states in complexes of iron oxophlorin is clearly shown by our theoretical data. To explain this effect, a simple qualitative d-orbital splitting scheme for the possible π-interactions along the *z* molecular axis of $[R_{Py}]$ is presented in Figure 7. In the middle (panel A), no π-interactions between

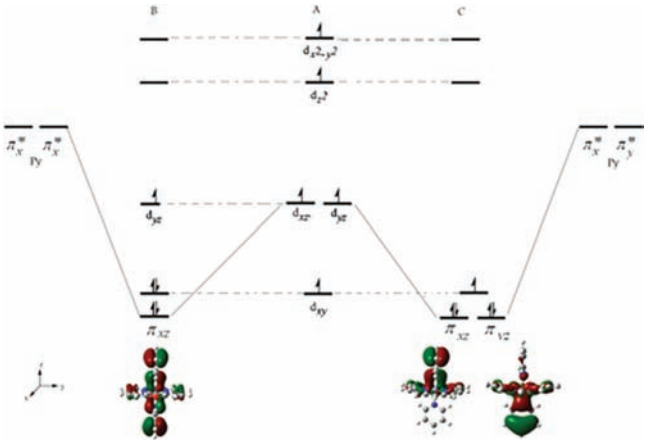

Figure 7. Molecular orbital diagram illustrating the possible π-intractions of axial pyridine ligands with (d_{xz}, d_{yz}) iron orbital in low-spin R_{Py}: (A) no π-bonding along the *z*-axis, (B) π-bonding with a single d_{xz}, and (C) π-bonding with both d_{xz} and d_{yz} orbitals.

(d_{xz}, d_{yz}) orbitals and axial ligands are assumed, whereas Por−metal π-bonds are considered to be present.[44] For a perfect matching of the π orbitals of the axial ligands with the metal $\pi(d_{xz}, d_{yz})$ orbitals, and, based on the relative orientations of the pyridine planes, two idealized forms (panels B and C) may be envisioned.

In configuration B in the figure, the pyridine planes are coplanar and only the d_{xz} orbital of Fe(III) overlaps with both the empty π^* orbital of pyridine. Clearly such unsymmetrical π-bonding between Fe(III) dπ orbitals and the axial ligand π-systems will remove the degeneracy of the d_{xz}, d_{yz} orbitals. In the C form pyridine planes are perpendicular and both degenerate orbitals d_{xz} and d_{yz} of Fe(III) donate electron density into the π^*_x and π^*_y orbitals of axial ligands. In accordance with Figure 7, it might be anticipated that a low-spin $^2R_{Py}$ with configuration B in Figure 7, $\pi_{xz}^2 d_{xy}^2 d_{yz}^1$ and Fe−N_{ax}= 2.06 Å is present for parallel pyridines and a low spin with configuration C shown in 7, $\pi_{xz}^2 \pi_{yz}^2 d_{xy}^1$ and Fe−N_{ax}= 2.03 Å were seen for the perpendicular ones.

The Relevancy of Electronic Configuration with Crossover Spin Property. In contrast to $^2R_{Im}$, *t*-BuNC and pyridine as axial ligands with stronger π-accepting ability stabilize the $(\pi_{xz}\ \pi_{yz})^4 d_{xy}^1$.[45] The energy gap between the d_{xy} and dπ orbitals of Fe in $R_{t\text{-BuNC}}$ is always larger than that of complex $^2R_{Py}$. Thus, it is clear that the ligand of (*t*-BuNC) stabilizes the $(\pi_{xz}\ \pi_{yz}^4) d_{xy}^1$ ground state more than pyridine.

Figure 8 presents ground-state frontier MO energy-level diagrams for complexes R_{Im}, R_{Py}, and $R_{t\text{-BuNC}}$, respectively. The axial ligand of imidazole with a strong σ-donating and weak π-accepting ability causes the $^2R_{Im}$ complexes to adopt the $d_{xy}^2 (\pi_{xz}\ \pi_{yz})^3$ ground state. In $^2R_{Py}$ and $^2R_{t\text{-BuNC}}$, with much better

dx.doi.org/10.1021/ic202527u | *Inorg. Chem.* 2012, 51, 7094−7102

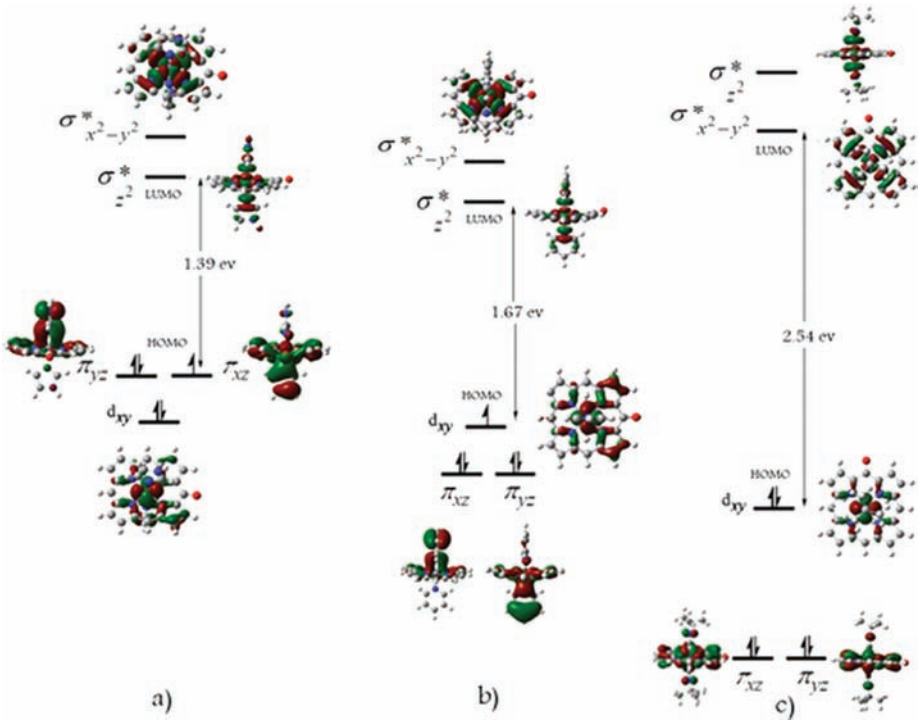

Figure 8. OPBE MO energy level (eV) diagram for ground state ($s = {}^1/_2$) (a) R_{Im}, (b) R_{Py}, and (c) $R_{t\text{-BuNC}}$.

π-accepting ability of the ligands to that of pyridine, the ground-state $(\pi_{xz}\,\pi_{yz})^4\,d_{xy}^1$ electronic configuration is observed.

Figure 8 also shows that HOMO−LUMO gap of R_{Im} (OPBE 1.39 eV, B3LYP 1.25 eV), R_{Py} (OPBE 1.67 eV, B3LYP 1.53 eV), and $R_{t\text{-BuNC}}$ (OPBE 2.54 eV, B3LYP 2.28 eV) span a remarkably wide range of ∼1 eV. These results provide some of the first insight into just how dramatically the axial ligands can tune the HOMO−LUMO gaps and, hence, the spin-state energetics of iron oxophlorin complexes. The HOMO−LUMO gaps provide a qualitative explanation of why the experimental analogue of $^2R_{Im}$, which has low-energy excited states with ($s = {}^3/_2$ and $s = {}^5/_2$), exhibits spin crossover behavior with temperature. The diagram presented in Figure 8 also indicates why such behavior would be out of the question for $^2R_{t\text{-BuNC}}$.

Therefore, the $^2R_{Im}$ complex shows temperature-dependent increases in its magnetic moments, which are likely to result from the occupation of an $s = {}^5/_2$ or a spin-admixed $s = {}^5/_2, {}^3/_2$ state at higher temperatures, while the magnetic moment of $R_{t\text{-BuNC}}$ is temperature-invariant and consistent with a doublet state.[29] The population of closely lying excited spin state (quartet) in $^2R_{Im}$ (with perpendicular imidazole) favors rotation of one axial ligand to form $^4R_{Im}$ (with parallel imidazole) which favors the quartet ground state (see Figure 5). In the complexes of $R_{t\text{-BuNC}}$ and R_{Py} with the $(\pi_{xz}\,\pi_{yz})^4\,d_{xy}^1$ ground state, the unpaired electron in the d_{xy} orbital can be delocalized to the ring, especially on the meso-C atoms, by interaction with the oxophlorin a_{2u} orbital. There is significant delocalization of the unpaired electron from the oxophlorin a_{2u} orbital to the Fe d_{xy} orbital. In the $(\pi_{xz}\,\pi_{yz})^4\,d_{xy}^1$ configuration, if the d_{xy} orbital is located far above the $d\pi$ orbital in the energy diagram, the complex has a very pure $(\pi_{xz}\,\pi_{yz})^4\,d_{xy}^1$ ground state (such as $R_{t\text{-BuNC}}$). If, on the other hand, the energy difference is rather small, then the contribution of the excited state increases (such as R_{Py}) (see Figure 2).

Therefore, the stability of the $(\pi_{xz}\,\pi_{yz})^4\,d_{xy}^2\,a_{2u}^1$ ground state increases as the axial ligand changes from Im to t-BuNC in the other, which can be given as follows:

$$\text{Im} < \text{Py} < t\text{-BuNC}$$

Electronic Structure of the Oxophlorin Radical. At higher temperatures, the $^2R_{Py}$ complexes produce relatively stable free radicals in which the odd electron is largely delocalized on the tetrapyrrole macrocycle and in the $R_{t\text{-BuNC}}$ complex, one of the electrons is totally shifted from the oxophlorin ring to iron, which results in the free-radical species localized on the oxophlorin. Figure 4 shows the singly occupied molecular orbital (SOMO), which corresponds to the well-known porphyrin a_{2u} orbital and is populated at temperatures above 273 K.[24] Table 3 shows that the spin density within the radical is, especially at the oxygen atom (spin density on the ketone oxygen atom is 0.27) with significant spin density at the *meso* carbons (spin density on the meso carbon is 0.13), highest at the *meso* carbon trans to the oxygen atom (the spin density on the *meso* carbon trans to the oxygen atom is 0.30). The electronic effect of ethyl groups instead of hydrogens has been also shown in Figure 4, which shows very similar electron distributions in both. Therefore, the replacement of ethyl groups by hydrogens has no significance on the reliability of the calculation.

The spin densities on the β-pyrrole positions also varies from −0.02 to 0.07 in the a_{2u} HOMO orbitals. ^{1}H NMR of the $[(py)_2Fe(OEPO)]$ in py-d_5 reported by Moroshima shows large contacts shifts for meso protons and widespread CH_2 signals. These spin delocalizations and variations obtained by DFT calculation (see Figure 4b) are in very good agreement with the ^{1}H NMR data reported for $[(py)_2Fe(OEPO)]$ by Morishima[46] and Balch.

The $^2[R_{py}]_{xy}$ is a doublet state with a singly occupied d_{xy} orbital. As the temperature increases, one of the electrons is promoted to a singly occupied d_{xy} orbital ($a_{2u}\rightarrow d_{xy}$), which

dx.doi.org/10.1021/ic202527u | Inorg. Chem. 2012, 51, 7094−7102

results in the free-radical species of $^2[R_{Py}]_{a2u}$ (see Figure 2), thereby allowing an increase in spin density at the *meso* carbons. Therefore, changing the electronic state of $^2[R_{py}]_{xy}$ to $^2[R_{py}]_{a2u}$ by temperature could be responsible for non-Curie law behavior in the ^{1}H NMR reported for [(py)$_2$Fe(OEPO)] by Morishima.[46]

In these transformations, reactivity is directed, as expected, to the sites of highest spin density. Oxidation at the *meso* carbon trans to the oxygen atom was seen in the model reaction, but it seems that, in heme oxygenase, the related reaction was prohibited by steric hindrance.[24]

Thus, the radical nature of the macrocycle in R_{Py} and $R_{t\text{-BuNC}}$ makes them air-sensitive and they readily undergo opening of the oxophlorin ligand to produce verdoheme. However, it seems that, at low temperatures, R_{Py} has an electronic configuration of $\pi_{xz}^2\ \pi_{yz}^2\ a_{2u}^2\ d_{xy}^1$ and should be considerably less reactive toward O_2.

In summary, the axial ligand has a major effect on the high-lying occupied and low-lying virtual orbitals of $[L_2\ Fe\ (PO)]^0$, whereby the orbital energy levels shift in energy, depending on the nature of the axial ligand. Because the latter orbital is the HOMO, this also affects the electron abstraction ability of the oxidant.

CONCLUSION

Axial ligands have profound effects on the electronic configuration, oxidation, spin states, and reactivity of the iron oxophlorines. When the axial ligands are strong σ donators and π acceptors such as CN or CNR, the iron is in the oxidation state of 2 and is diamagnetic, $(\pi_{xz},\ \pi_{yz})^4\ d_{xy}^2\ a_{2u}^1$. The oxophlorin ring has a radical nature with spin delocalization on the oxygen and *meso* carbon adjacent to it. This electronic and spin delocalization on the ring is the key to the reactivity of the ring toward dioxygen.

When the axial ligand changed to the intermediate ligands, with regard to the σ donating and π ability (such as pyridines), the ground-state electronic configuration is $\pi_{xz}^2\ \pi_{yz}^2\ a_{2u}^2\ d_{xy}^1$ in low temperature and $\pi_{xz}^2\ \pi_{yz}^2\ d_{xy}^2\ a_{2u}^1$ in high temperature. Therefore, the macrocycle is not reactive toward O_2 in low temperatures but is reactive in higher temperatures.

With weak π accepting ligands such as imidazole, the iron oxophlorin has doublet ground state with a singly occupied π_{xz} orbital. The low-lying excited state is a quartet just 2.32 kcal/mol above the ground state. In these cases, spin crossover occurs readily, but the ring is predicted to be less reactive.

ASSOCIATED CONTENT

Supporting Information

This material is available free of charge via the Internet at http://pubs.acs.org.

AUTHOR INFORMATION

Corresponding Author

*Tel.: + 98-21-22401765. Fax: + 98-21-22403041. E-mail: n-safari@cc.sbu.ac.ir.

Notes

The authors declare no competing financial interest.

ACKNOWLEDGMENTS

We are grateful to Prof. S.W. Ng for providing us the software Gaussian suite of programs and hardware (machine time) facilities and also for providing us the opportunity to access some new features of Gaussian products. The authors would like to acknowledge financial support from the Research Council of Shahid Beheshti University. Also technical support of the Chemistry Computational Center at Shahid Beheshti University is greatly acknowledged.

REFERENCES

(1) Ortiz de Montellano, P. R.; Auclair, K. In *The Porphyrin Handbook*, Vol. 12; Kadish, K. M., Smith, K. M., Guilard, R., Eds.; Academic Press: New York, CA, 2003; pp 183−210.
(2) Sono, M.; Roach, M. P.; Coulter, E. D.; Dawson, J. H. *Chem. Rev.* **1996**, *96*, 2841−2888.
(3) Kikuchi, G.; Yoshida, T. *Trends Biochem. Sci.* **1980**, *5*, 323−325.
(4) Bonnett, R.; Dimsdale, M. J. *J. Chem. Soc., Perkin Trans. 1* **1972**, 2540−2548.
(5) Fuhrhop, J. H.; Besecke, S.; Subramanian, J. *J. Chem. Soc., Chem. Commun.* **1973**, 1−2.
(6) Balch, A. L. *Coord. Chem. Rev.* **2000**, *200−202*, 349−377.
(7) Ortiz de Montellano, P. R. *Acc. Chem. Res.* **1998**, *31*, 543−549.
(8) Balch, A. L.; Noll, B. C.; Zovinka, E. P. *J. Am. Chem. Soc.* **1992**, *114*, 3380−3385.
(9) Balch, A. L.; Latos-Grazynski, L.; Noll, B. C.; Olmstead, M. M.; Szterenberg, L.; Safari, N. *J. Am. Chem. Soc.* **1993**, *115*, 1422−1429.
(10) Zhang, X.; Fujii, H.; Matera, K. M.; Migita, C. T.; Sun, D.; Sato, M.; Ikeda-Saito, M.; Yoshida, T. *Biochemistry* **2003**, *42*, 7418−7426.
(11) Lad, L.; Ortiz de Montellano, P. R.; Poulos, T. L. *J. Inorg. Biochem.* **2004**, *98*, 1686−1695.
(12) Lad, L.; Friedman, J.; Li, H.; Bhaskar, B.; Ortiz de Montellano, P. R.; Poulos, T. L. *Biochemistry* **2004**, *43*, 3793−3801.
(13) Kikuchi, G.; Yoshida, T.; Noguchi, M. *Biochem. Biophys. Res. Commun.* **2005**, *338*, 558−567.
(14) Tanaka, R.; Kowase, S.; Unno, M. *Dalton Trans.* **2010**, *39*, 9235−9237.
(15) Matsui, T.; Unno, M.; Ikeda-Saito, M. *Acc. Chem. Res.* **2009**, *43*, 240−247.
(16) Balch, A. L.; Latos-Grazynski, L.; Noll, B. C.; Olmstead, M. M.; Safari, N. *J. Am. Chem. Soc.* **1993**, *115*, 9056−9061.
(17) Batch, A. L.; Koerner, R.; Olmstead, M. M.; Mazzanti, M.; Safari, N.; Claire, T. *J. Chem. Soc., Chem. Commun.* **1995**, 643−644.
(18) Hildebrand, D. P.; Tang, H.-l.; Luo, Y.; Hunter, C. L.; Smith, M.; Brayer, G. D.; Mauk, A. G. *J. Am. Chem. Soc.* **1996**, *118*, 12909−12915.
(19) Gheidi, M.; Safari, N.; Bahrami, H.; Zahedi, M. *J. Inorg. Biochem.* **2007**, *101*, 385−395.
(20) Bahrami, H.; Zahedi, M.; Safari, N. *J. Inorg. Biochem.* **2006**, *100*, 1449−1461.
(21) Jamaat, P.; Safari, N.; Ghiasi, M.; Naghavi, S.; Zahedi, M. *J. Biol. Inorg. Chem.* **2008**, *13*, 121−132.
(22) Gheidi, M.; Safari, N.; Zahedi, M. *J. Mol. Model.* **2010**, *16*, 1401−1413.
(23) Lai, W.; Chen, H.; Matsui, T.; Omori, K.; Unno, M.; Ikeda-Saito, M.; Shaik, S. *J. Am. Chem. Soc.* **2010**, *132*, 12960−12970.
(24) Balch, A. L.; Latos-Grażyński, L.; Noll, B. C.; Szterenberg, L.; Zovinka, E. P. *J. Am. Chem. Soc.* **1993**, *115*, 11846−11854.
(25) Balch, A. L.; Koerner, R.; Latos-Grażyński, L.; Noll, B. C. *J. Am. Chem. Soc.* **1996**, *118*, 2760−2761.
(26) Kalish, H.; Camp, J. E.; Stępień, M.; Latos-Grażyński, L.; Balch, A. L. *J. Am. Chem. Soc.* **2001**, *123*, 11719−11727.
(27) Rath, S. P.; Olmstead, M. M.; Balch, A. L. *Inorg. Chem.* **2004**, *43*, 7648−7655.
(28) Rath, S. P.; Olmstead, M. M.; Balch, A. L. *J. Am. Chem. Soc.* **2004**, *126*, 6379−6386.
(29) Rath, S. P.; Olmstead, M. M.; Balch, A. L. *Inorg. Chem.* **2006**, *45*, 6083−6093.
(30) Siegbahn, P. E. M. *Faraday Discuss.* **2003**, *124*, 289−296.
(31) Frisch, M. J.; Trucks, G. W.; Schlegel, H. B.; Scuseria, G. E.; Robb, M. A.; Cheeseman, J. R.; Zakrzewski, V. G.; Montgomery, J. A.; Stratmann, R. E.; Burant, J. C.; Dapprich, S.; Millam, J. M.; Daniels, A.

D.; Kudin, K. N.; Strain, M. C., Farkas, O, Tomasi, J, Barone, V, Cossi, M, Cammi, R,Mennucci, B, Pomelli, C, Adamo, C, Clifford, S., Ochterski, J.; Petersson, G. A.; Ayala, P. Y.; Cui, Q.; Morokuma, K.; Malick, D. K.; Rabuck, A. D.; Raghavachari, K.; Foresman, J. B.; Cioslowski, J.; Ortiz, J. V.; Stefanov, B. B.; Liu, G.; Liashenko, A.; Piskorz, P.; Komaromi, I.; Gomperts, R.; Martin, R. L.; Fox, D. J.; Keith, T.; Al-Laham, M. A.; Peng, C. Y.; Nanayakkara, A.; Ghonzalez, C. V.; Challacombe, M. W.; Gill, P. M.; Johnson, B. G.; Chen, W.; Wong, M.; Andres, J. L.; Head-Gordon, M.; Replogle, E. S.; Pople, J. A. *Gaussian 03 (Revision A.1)*; Gaussian: Pittsburgh, PA, 2003.

(32) Parr, R. G.; Yang, W. *Density-Function Theory of Atoms and Molecules*; Oxford University Press: Oxford, U.K., 1989.

(33) Cramer, C. J. *Essentials of Computational Chemistry: Theories and Models*; Wiley: Chichester, U.K., 2002.

(34) Swart, M. *J. Chem. Theory Comput.* **2008**, *4*, 2057−2066.

(35) Güell, M.; Luis, J. M.; Solà, M.; Swart, M. *J. Phys. Chem. A* **2008**, *112*, 6384−6391.

(36) Lee, C.; Yang, W.; Parr, R. G. *Phys. Rev. B* **1988**, *37*, 785−789.

(37) Vosko, S. H.; Wilk, L.; Nusair, M. *Can. J. Phys.* **1980**, *58*, 1200−1211.

(38) Stephens, P. J.; Devlin, F. J.; Chabalowski, C. F.; Frisch, M. J. *J. Phys. Chem.* **1994**, *98*, 11623−11627.

(39) Yoshizawa, K.; Kamachi, T.; Shiota, Y. *J. Am. Chem. Soc.* **2001**, *123*, 9806−9816.

(40) Shiota, Y.; Yoshizawa, K. *J. Am. Chem. Soc.* **2000**, *122*, 12317−12326.

(41) Ghosh, A. *J. Biol. Inorg. Chem.* **2006**, *11*, 671−673.

(42) Ghosh, A. *J. Biol. Inorg. Chem.* **2006**, *11*, 712−724.

(43) Tangen, E.; Conradie, J.; Ghosh, A. *J. Chem. Theory Comput.* **2007**, *3*, 448−457.

(44) La Mar, G. N.; Walker, F. A. *J. Am. Chem. Soc.* **1975**, *97*, 5103−5107.

(45) Ikeue, T.; Handa, M.; Chamberlin, A.; Ghosh, A.; Ongayi, O.; Vicente, M. G. H.; Ikezaki, A.; Nakamura, M. *Inorg. Chem.* **2011**, *50*, 3567−3581.

(46) Morishima, I.; Fujii, H.; Shiro, Y.; Sano, S. *J. Am. Chem. Soc.* **1986**, *108*, 3858−3860.